www.acsnano.org

Negative Thermal Quenching in Quantum-Cutting Yb^{3+} -Doped $CsPb(Cl_{1-x}Br_x)_3$ Perovskite Nanocrystals Joo Yeon D. Roh, Tyler J. Milstein, and Daniel R. Gamelin*



Downloaded via UNIV OF WASHINGTON on October 16, 2023 at 17:03:24 (UTC). See https://pubs.acs.org/sharingguidelines for options on how to legitimately share published articles.

Cite This: ACS Nano 2023, 17, 17190-17198



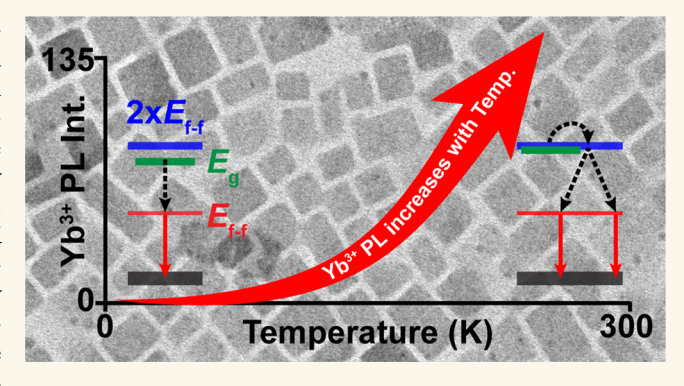
ACCESS |

III Metrics & More

Article Recommendations

Supporting Information

ABSTRACT: Ytterbium-doped all-inorganic lead-halide perovskites $(Yb^{3+}:CsPb(Cl_{1-x}Br_x)_3)$ show broadband absorption and exceptionally high near-infrared photoluminescence quantum yields, providing opportunities for solar spectral shaping to improve photovoltaic power conversion efficiencies. Here, we report that $Yb^{3+}:CsPb(Cl_{1-x}Br_x)_3$ NCs also show extremely strong negative thermal quenching of the Yb^{3+} luminescence, with intensities at room temperature >100 times those at 5 K for some compositions. Analysis of this temperature dependence as a function of x shows that it stems from thermally activated quantum cutting related to the temperature dependence of the spectral overlap between the PL of the perovskite (donor) and the simultaneous-pair absorption of two Yb^{3+} ions



(acceptor). In the Yb³+:CsPbBr₃ limit, this spectral overlap goes to zero at 5 K, such that only single-Yb³+ sensitization requiring massive phonon emission occurs. At room temperature, Yb³+ PL in this composition is enhanced ~135-fold by thermally activated quantum cutting, highlighting the extreme efficiency of quantum cutting relative to single-Yb³+ sensitization. These results advance the fundamental mechanistic understanding of quantum cutting in doped perovskites, with potential ramifications for solar and photonics technologies.

KEYWORDS: quantum cutting, ytterbium doping, energy transfer, negative thermal quenching, perovskites

ptoelectronic materials that promote photomultiplication (e.g., singlet fission, carrier multiplication, and quantum cutting)1-5 have attracted broad interest because of their potential to improve upon the Shockley-Queisser thermodynamic limit of single-junction photovoltaics.^{6–8} Quantum cutting, like singlet fission and carrier multiplication, splits the energies of single absorbed solar photons to generate multiple lower-energy excitations that, in principal, may be used to generate additional photocurrent and reduce thermalization losses. 9,10 Ytterbium-doped all-inorganic lead-halide perovskites (Yb3+:CsPb(Cl1-xBrx)3) have demonstrated extremely efficient quantum cutting, in some cases achieving photoluminescence quantum yields (PLQYs) approaching 200%. 11-13 Unlike quantum cutting in other materials, Yb^{3+} :CsPb($Cl_{1-x}Br_x$)₃ quantum cutting involves broadband absorption by a direct-band-gap semiconductor, allowing efficient harvesting of solar photons. The nearinfrared (NIR) Yb3+ emission that results from quantum cutting also aligns very well with the maximum energyconversion efficiency of crystalline Si photovoltaics. 11-26 These attractive properties have motivated both fundamental and

applied investigations into these materials in the forms of colloidal nanocrystals (NCs), $^{11,13-16,18-23,25,26}$ single crystals, 25 and solution-processed and vapor-deposited thin films. 12,17,24

A critical factor in Yb³⁺:CsPb(Cl_{1-x}Br_x)₃ quantum cutting is the energy of the perovskite's lowest excited state relative to that of the Yb³⁺ ff excited states. Narrowing the perovskite energy gap ($E_{\rm g}$) in Yb³⁺:CsPb(Cl_{1-x}Br_x)₃ by increasing x from 0.00 (CsPbCl₃) to 1.00 (CsPbBr₃) initially has little effect but then results in dramatic loss of Yb³⁺ photoluminescence (PL) intensity as $E_{\rm g}$ crosses approximately twice the energy of the Yb³⁺ (2 F_{7/2} \rightarrow 2 F_{5/2}) absorption (2 × E_{f-p} ~20500 cm⁻¹).²⁰

Received: June 5, 2023 Accepted: August 14, 2023 Published: August 22, 2023





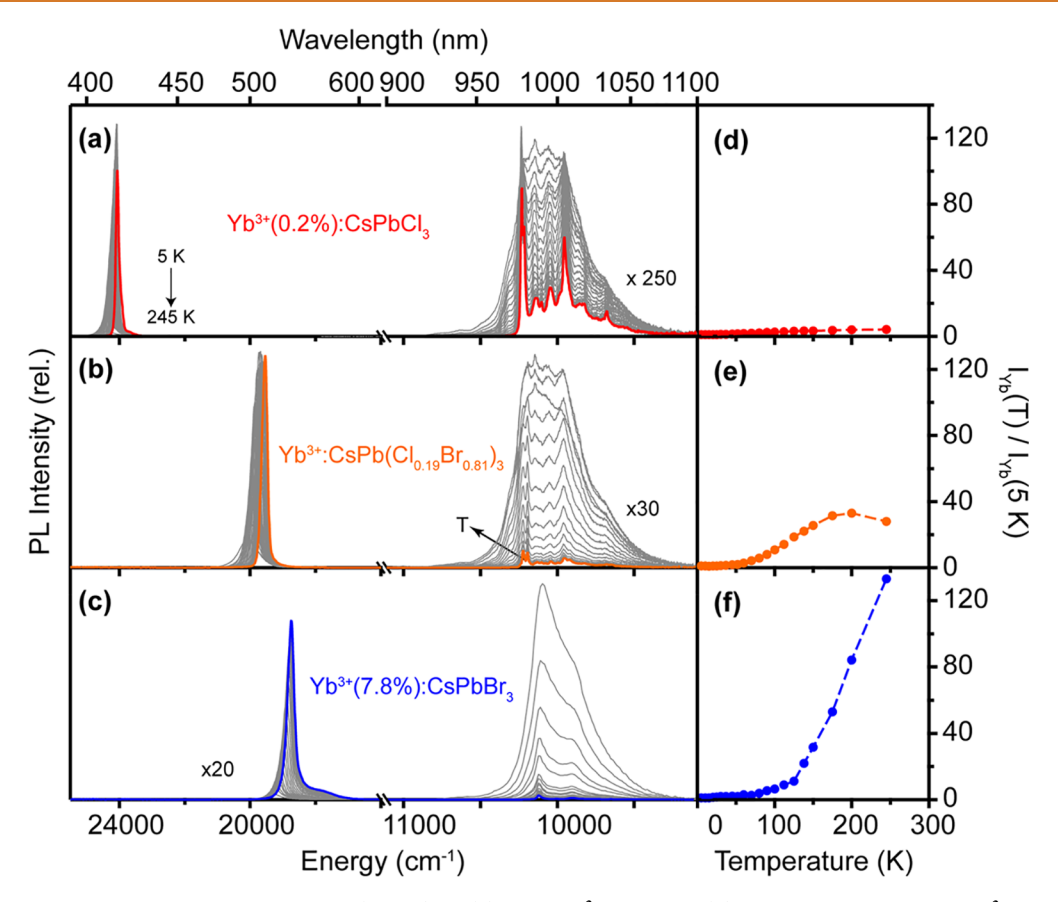


Figure 1. Variable-temperature photoluminescence (VTPL) of (a) 0.2% Yb³⁺:CsPbCl₃, (b) anion-exchanged 0.2% Yb³⁺:CsPb(Cl_{0.19}Br_{0.81})₃, and (c) 7.8% Yb³⁺:CsPbBr₃ NCs from 5 (colored) to 245 K. (d-f) Integrated Yb³⁺ PL intensity at each temperature point relative to 5 K ($I_{Yb}(T)/I_{Yb}(5 \text{ K})$) is plotted as a function of temperature for each sample from panels (a-c). All measurements used CW excitation at λ_{ex} = 375 nm (26700 cm⁻¹).

This behavior was interpreted as reflecting a thermodynamic threshold for energy-conserving quantum cutting.

Here, we report results from variable-temperature photoluminescence (VTPL) and absorption studies of Yb³⁺:CsPb- $(Cl_{1-x}Br_x)_3$ (0.00 $\leq x \leq 1.00$) NCs that reveal very large negative thermal quenching, a phenomenon involving increasing PL intensity with increasing temperature, in contrast to the common observation of thermally activated quenching via nonradiative multiphonon decay. Negative thermal quenching of Yb3+ PL is shown to depend systematically on anion alloying in Yb3+:CsPb(Cl1-xBrx)3 NCs, increasing dramatically with increasing x and reaching a \sim 135× intensity increase between 5 and 295 K for x = 1.00. We show that this negative thermal quenching stems from a strong temperature dependence of the donor-acceptor spectral overlap between perovskite PL and Yb3+-Yb3+ simultaneous-pair absorption spectra that governs quantum cutting due to both the anti-Varshni shift in E_g and thermal spectral broadening. In the extreme case, we show that quantum cutting is fully suppressed at 5 K for Yb³⁺:CsPbBr₃ NCs (x = 1.00), allowing detection of the competing single-Yb³⁺ energy-transfer process that is otherwise obscured in the presence of quantum cutting. This process requires massive phonon emission to release ~10000 cm⁻¹ excess energy per energy-transfer event, and large increases in the Yb3+ internal temperature are observed.

The negative thermal quenching reported here is anomalously large for doped perovskites. Previous work has shown that Yb³⁺ PL intensities in Yb³⁺:CsPbCl₃ NCs increase by a

modest factor of ~3 upon heating from 5 to 298 K^{13,25} and that Er³⁺ PL in Yb³⁺/Er³⁺ codoped CsPbCl₃ NCs and thin films also shows similar increases, ^{27,28} but the effect of Br alloying on such PL temperature dependence has never been examined. Indeed, Yb³⁺:CsPb(Cl_{1-x}Br_x)₃ samples with $E_{\rm g} < 2 \times E_{f-f}$ have received virtually no attention at all, and, for example, neither the PL temperature dependence nor even the low-temperature Yb³⁺ PL spectrum of Yb³⁺:CsPbBr₃ has been reported. The findings presented here advance our mechanistic understanding of Yb³⁺ sensitization in these extraordinary materials, thereby aiding their potential future applications in solar or other technologies.

RESULTS AND DISCUSSION

Yb³⁺:CsPb(Cl_{1-x}Br_x)₃ Nanocrystal Synthesis, Characterization, and Anion-Exchange Chemistry. Yb³⁺:CsPbCl₃ NCs were prepared by hot-injection using trimethylsilyl chloride (TMS-Cl) as the halide source, as reported previously (see Methods). 13,18,20,25 Yb³⁺:CsPb(Cl_{1-x}Br_x)₃ NCs with x up to 1.00 were prepared from these Yb³⁺:CsPbCl₃ NCs by postsynthetic anion exchange using trimethylsilyl bromide (TMS-Br). $^{29-31}$ Yb³⁺:CsPbBr₃ NCs were also synthesized directly by hot-injection of TMS-Br. X-ray diffraction and transmission electron microscopy (TEM) data for these NCs resemble those reported previously, all showing rectangular shapes with average edge lengths of \sim 14–17 nm and powder diffraction that agrees well with the

reference perovskite crystal structures with no detectable crystalline impurities (Figures S1 and S2).

The Effects of Anion Exchange on Yb3+:CsPb- $(Cl_{1-x}Br_x)_3$ Nanocrystal Photoluminescence. Figure 1 plots exciton and Yb3+ PL spectra for 0.2% Yb3+:CsPbCl3, 0.2% Yb³⁺:CsPb(Cl_{1-x}Br_x)₃ NCs at various anion compositions (x), and 7.8% Yb3+:CsPbBr3 NCs, each measured at several temperatures from 5 to 295 K using continuous-wave (CW) excitation. Due to the low dopant concentrations used in Figure 1a,b, the excitonic PL is substantially stronger than the Yb3+ PL in some of these spectra, and the NIR region has been magnified in the figure (250 and 30×) for clarity. At 5 K, the Yb^{3+ 2}F_{5/2} \rightarrow ²F_{7/2} PL of the Yb³⁺:CsPbCl₃ NCs (Figure 1a) shows several resolved features, as previously reported. 13,25 Elevating the temperature broadens these features and causes an increase in the integrated NIR PL intensity (i.e., negative thermal quenching) until near room temperature, where nonradiative relaxation is sometimes observed to decrease the intensities again. In concert, the excitonic PL intensities gradually decrease with increasing temperature, accompanied by the expected anti-Varshni blue shifts. 13,32,33 Note that the onset and magnitude of the Yb3+ PL intensity decrease at high temperature varies from sample to sample (e.g., it is not observed in the 3.5% and 7.8% Yb3+:CsPb(Cl1-xBrx)3 NCs of this study, Figures S7 and S8), 13,25 and it is therefore not considered further in our analysis. Figure 1d-f summarizes this Yb³⁺ PL temperature dependence by plotting the integrated NIR PL intensities at each temperature relative to the 5 K NIR PL intensities of the same sample $(I_{Vb}(T)/I_{Vb}(5 \text{ K}))$.

Although the same general trends are observed for all Yb³⁺:CsPb(Cl_{1-x}Br_x)₃ NC samples, a striking observation from Figure 1 is that the level of negative thermal quenching of Yb³⁺ increases dramatically as x increases. For example, Figure 1 shows that the Yb³⁺ PL intensity in Yb³⁺:CsPbCl₃ NCs increases roughly 4× going from 5 to 245 K, whereas that of the Yb³⁺:CsPbBr₃ NCs increases by >135×. These data also reveal that the onset of Yb³⁺ negative thermal quenching systematically shifts to a higher temperature with increasing x (e.g., from ~5 K in Yb³⁺:CsPbCl₃ NCs (Figure 1d) to ~150 K in Yb³⁺:CsPbBr₃ NCs (Figure 1f)).

The observations described in Figure 1 are summarized in a different way in Figure 2. Three series of Yb^{3+} : $CsPb(Cl_{1-x}Br_x)_3$ $(0.00 \le x \le 1.00)$ NCs, having [Yb³⁺] = 7.8%, 3.5%, and 0.2%, respectively, were prepared by extracting sample aliquots during stepwise partial anion-exchange reactions, and VTPL data were measured for each sample (Figures S7-S9). Figure 2a plots the integrated Yb³⁺ PL intensities for each sample measured at room temperature as a function of the sample's excitonic PL energy measured at the same temperature. The data collected at 5 K are also plotted in the same way. At room temperature, the Yb³⁺ PL intensity of the initial Yb³⁺:CsPbCl₃ NCs is retained upon partial anion exchange but decreases rapidly when $E_{\rm g} \approx 20000~{\rm cm}^{-1}$. These room-temperature data follow precisely the trend reported previously, 20 summarized by the dashed curve in Figure 2a. We previously interpreted this trend as reflecting the existence of a quantum-cutting energy threshold, defined by $E_{\rm g} \approx 2 \times E_{f-f}^{20}$ Above this threshold $(E_g > 2 \times E_{f-f})$, quantum cutting is exothermic and can occur spontaneously, releasing excess energy as heat into the lattice. Below this threshold $(E_g < 2 \times E_{f-f})$, the excited perovskite possesses insufficient energy to excite two Yb³⁺ ions. The data in Figure 2a show that decreasing from 295 to 5 K shifts the apparent threshold ~ 750 cm⁻¹ higher in energy.

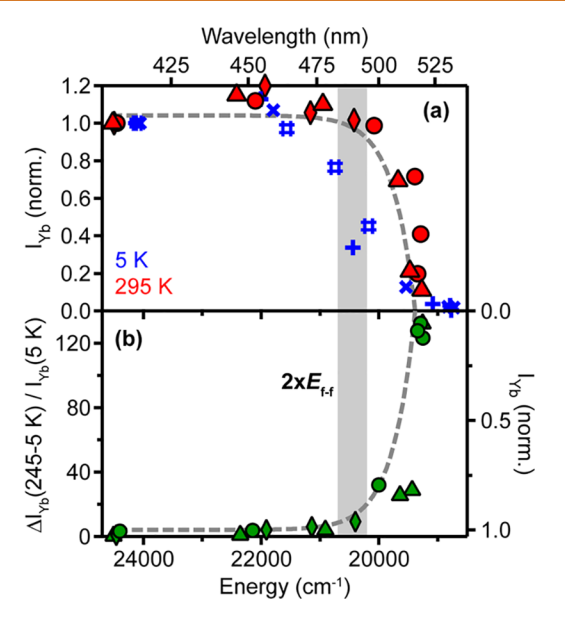


Figure 2. (a) Integrated Yb³⁺ (${}^{2}F_{5/2} \rightarrow {}^{2}F_{7/2}$) PL intensities of (i) 0.2% Yb3+:CsPbCl3 and anion-exchanged Yb3+:CsPb(Cl1-xBrx)3 NCs, and 7.8% Yb3+:CsPbBr3 NCs, taken from Figures 1 and S9 (and +), (ii) 3.5% Yb3+:CsPbCl3 and anion-exchanged Yb³⁺:CsPb(Cl_{1-x}Br_x)₃ NCs from Figure S8 (\spadesuit and #), (iii) 7.8% Yb3+:CsPbCl3 and anion-exchanged Yb3+:CsPb(Cl1-xBrx)3 NCs, and 5.5% Yb3+:CsPbBr3 NCs from Figure S7 (▲ and ×), all measured at room temperature (solid red marks) and at 5 K (open blue marks). Data are plotted vs the exciton PL energy measured at the same temperature, equated with E_{g} . The gray dashed line reproduces the experimental trend at room temperature reported in ref 20, showing good agreement. Data for each anion-exchange series are normalized to the Yb3+:CsPbCl3 NC data point of that series, and data points for independently synthesized Yb³⁺:CsPbBr₃ NCs are scaled to match the Yb³⁺:CsPb(Cl_{1-x}Br_x)₃ NC trends in the limit of x = 1.00. (b) Change in Yb³⁺ PL intensity from 5 to 245 K normalized by the 5 K intensity $(\Delta I_{Yb}(245-5 \text{ K})/$ $I_{Yb}(5 \text{ K})$ for the samples in Figure 2a, plotted vs E_g at 245 K for each sample. The vertical gray bar indicates approximately twice the Yb³⁺ (${}^{2}F_{7/2} \rightarrow {}^{2}F_{5/2}$) absorption threshold (2 × E_{ff}), representing the proposed quantum-cutting energy threshold.

Notably, all three series of samples behave in the same way, showing that these trends are independent of the Yb³⁺ concentration.

The difference between the 295 and 5 K curves in Figure 2a emphasizes a central conclusion that can be drawn from these data, namely, that quantum cutting is strongly temperature dependent when E_g is near the quantum-cutting energy threshold. Figure 2b highlights the intimate relationship between the PL temperature dependence and the quantumcutting energy threshold by plotting the relative Yb3+ PL intensity increase from 5 to 245 K ($\Delta I_{Yb}(245-5 \text{ K})/I_{Yb}(5 \text{ K})$) vs the 245 K exciton PL energy ($E_o(245 \text{ K})$) from the Yb³⁺ PL data of Figures 1, S7-S9. This plot shows the same curvature as found in Figure 2a, only inverted (dashed curve). We note that although Yb³⁺:CsPbBr₃ NCs show $\Delta I_{Yb}(245-5 \text{ K})/I_{Yb}(5$ K) > 135, the Yb $^{3+}$ PL of this sample is actually extremely dim at all temperatures (Figures 2a, S7f, and S9f), meaning the increase in absolute Yb3+ PL intensity for this composition is still very small (Figure S13).

Having established the strong and systematic temperature dependence of Yb³⁺ PL intensities in the region where $E_{\rm g} \lesssim 2 \times E_{f,\theta}$ we now turn to clarifying the fundamental origins of this

temperature dependence, and specifically, we test the hypothesis that it ultimately reflects the changing efficiency of quantum-cutting energy transfer from the perovskite host (donor) to pairs of Yb³+ dopants (acceptors). An important factor in this efficiency is the quantum-cutting rate constant ($k_{\rm QC}$), which can be described within the general framework of Fermi's golden rule using eq 1. Here, $k_{\rm QC}$ is a function of the donor/acceptor electronic coupling ($M_{\rm DA}$) and the overlap (ρ) between the donor PL and acceptor absorption spectra.

$$k_{QC} = \frac{2\pi}{\hbar} |M_{DA}|^2 \rho \tag{1}$$

The data in Figure 2 speak primarily of the effect of changing $E_{\rm g}$ (through anion exchange) on ρ . To model ρ , we use the experimental near-band-edge PL as the donor emission spectrum for a given temperature and composition, including any contribution from dopant-induced defect states.³³ Previously, we have argued that quantum cutting in this system is concerted,¹³ in which case we may consider the acceptor to be a pair of Yb³⁺ ions (whether proximal or distal), and the final state in the energy-transfer process to be the pair's doubly excited $|^2F_{5/2}$, $^2F_{5/2}$) state. In Yb³⁺:CsPb(Cl_{1-x}Br_x)₃, experimental and computational results indicate that direct Yb³⁺-Yb³⁺ interactions are extremely weak, allowing the Yb³⁺-Yb³⁺ simultaneous pair absorption spectrum ($f_{\rm YbYb}$ in the visible energy region, x = 2y) to be generated from the single-Yb³⁺ absorption spectrum ($f_{\rm Yb}$ in the NIR energy region, y) using the convolution theorem (Supporting Information),^{34,35} as given by eq 2.

$$f_{YbYb}(x) = [f_{Yb}(y)]^2$$
 (2)

The donor/acceptor spectral overlap for Dexter-type energy transfer can then be quantified using the product of the areanormalized perovskite PL (g_{perov}) and Yb³⁺-Yb³⁺ pair absorption (f_{YbYb}) spectra as described by eq 3.^{36,37}

$$\rho = \int_0^\infty f_{YbYb}(x) g_{perov}(x) dx$$
(3)

Figure 3a plots the 5 K Yb³¹-Yb³¹ simultaneous-pair absorption spectrum obtained from the experimental NIR absorption spectrum of a pressed powder of 5.1% Yb³¹-CsPb-(Cl₀25Br₀,75)₃ NCs using eq 2, compared with the perovskite PL spectra collected at the same temperature for these NCs across the full anion-exchange series. Figure 3b shows analogous room-temperature data. We note that the Yb³¹- absorption spectrum is broader than its emission spectrum, which likely reflects the diverse speciation described previously. 25,38

Considering first the high-temperature results (Figure 3b), ρ is clearly very small at large E_g , but the data in Figure 2a show that quantum cutting is independent of ρ as long as $E_g > 2 \times E_{f,p}$ so eq 1 obviously does not fully account for the efficiency of quantum cutting; exothermic (phonon-emitting) quantum cutting in this range must be sufficiently rapid to outcompete other nonproductive relaxation channels. To account for this observation, ρ in eq 1 is replaced by the phenomenological parameter $P_{\rm OC}$, as described by eq 4.

$$P_{QC} = \int_0^c f_{YbYb}(x) g_{perov}(x) dx + \int_c^\infty f_{YbYb}(c) g_{perov}(x) dx$$
(4)

Here, c indicates the lowest energy at which 10% of the Yb³⁺-Yb³⁺ absorption maximum is reached (20230 and 20000

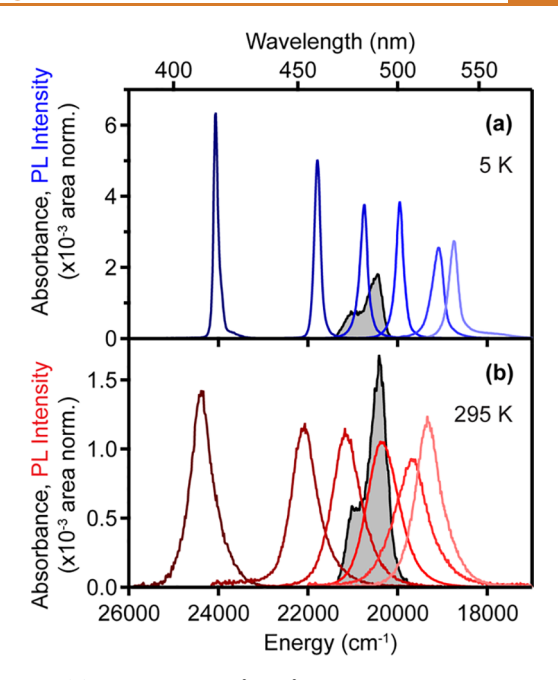


Figure 3. (a) Calculated Yb³+-Yb³+ simultaneous-pair absorption spectrum ($|^2F_{7/2}\rangle ^2F_{7/2}\rangle \rightarrow |^2F_{5/2}\rangle ^2F_{5/2}\rangle$, filled gray) for 5.1% Yb³+:CsPb(Cl_{0.25}Br_{0.75})₃ NC powder at 5 K, compared with experimental excitonic PL spectra of Yb³+:CsPb(Cl_{1-x}Br_x)₃ NCs also at 5 K. (b) Calculated Yb³+-Yb³+ simultaneous-pair absorption spectrum for 5.1% Yb³+:CsPb(Cl_{0.25}Br_{0.75})₃ NC powder at 295 K, compared with experimental excitonic PL spectra of Yb³+:CsPb(Cl_{1-x}Br_x)₃ NCs also at 295 K. All excitonic PL spectra and absorption spectra are area-normalized.

cm⁻¹ at 5 and 295 K, respectively, in Figure 3). For $x \le c$, $P_{\rm QC}$ is calculated as in eq 3. For x > c, $P_{\rm QC}$ is given by the integrated product of excitonic PL intensities and $f_{\rm YbYb}(c)$. The value of 10% is arbitrarily chosen to reproduce experiment at room temperature, but qualitatively similar results are obtained for other values up to ~75%. The effect of eq 4 is to account for efficient non-resonant energy transfer involving phonon emission. Using eq 4, the data in Figure 3 can be used to model the dependence of $I_{\rm Yb}$ on $E_{\rm g}$ shown in Figure 2a.

Figure 4a replots excitonic PL and Yb3+-Yb3+ simultaneouspair absorption spectra for 5.1% Yb3+:CsPb(Cl_{0.25}Br_{0.75})₃ NCs at 5 and 295 K from Figure 3 using an expanded x axis, highlighting the substantial change in spectral overlap for the same sample between these two temperatures. For this sample, $E_{\rm g}$ is smaller than 2 × $E_{\rm f-f}$ at 5 K but rises to ~2 × $E_{\rm f-f}$ with increasing temperature, accompanied by spectral broadening, dramatically increasing $P_{\rm QC}$. The Yb³⁺-Yb³⁺ pair absorption spectrum also broadens at an elevated temperature to a lesser extent. From these spectra, the application of eq 4 yields the values of P_{OC} indicated by the blue and red stars in Figure 4b (5 and 295 K, respectively). Notably, for the sample shown in Figure 4a, the spectral overlap increases ~11-fold between 5 and 295 K (i.e., $\Delta P_{QC}(295-5 \text{ K})/P_{QC}(5 \text{ K}) \approx 11$), which agrees well with the experimental value of $\Delta I_{Vb}(295-5 \text{ K})/$ $I_{Yb}(5 \text{ K}) = 12.5 \text{ measured for this sample (Figure S12)}.$ Similarly, P_{OC} values have been determined from the other spectra in Figure 3 as well as for other independent samples (Figure S14), and the results are plotted in Figure 4b as blue and red symbols (5 and 295 K, respectively) as a function of

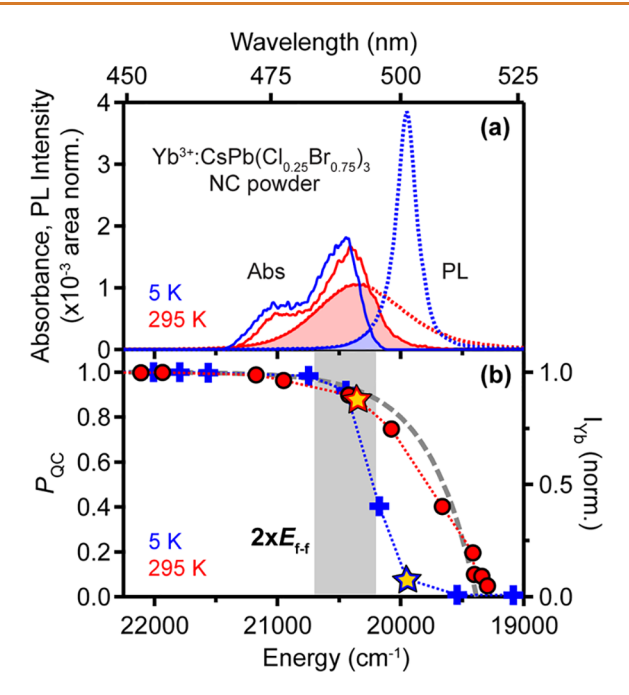


Figure 4. (a) Calculated Yb³+-Yb³+ simultaneous-pair absorption ($|^2F_{7/2}, ^2F_{7/2}\rangle \rightarrow |^2F_{5/2}, ^2F_{5/2}\rangle$, solid traces, calculated) and experimental excitonic PL (dotted traces) spectra of 5.1% Yb³+:CsPb(Cl_{0.25}Br_{0.75})₃ NC powder measured at 5 (blue) and 295 K (red). The filled areas correspond to the donor—acceptor spectral overlap at 5 (blue) and 295 K (pink). (b) Normalized values of the relative quantum-cutting energy-transfer probability (P_{QC}) at 5 (blue) and 295 K (red) calculated using eq 4 with the Yb³+-Yb³+ pair absorption spectra from panel (a) and excitonic PL spectra for Yb³+:CsPb(Cl_{1-x}Br_x)₃ (0.40 ≤ x ≤ 0.90) from Figures 3 and S14 (see Figure S16 for the full x range), plotted as a function of E_g at 5 and 295 K, respectively. The gray dashed line is taken from Figure 2a. Stars denote P_{QC} values calculated from the spectra in panel (a), highlighting the quantum-cutting temperature dependence.

The calculated results in Figure 4b agree well with the experimental data in Figure 2a, demonstrating that this analysis captures the essence of the experimental phenomenon. This analysis also explains the strong negative thermal quenching observed when $E_{\rm g} < 2 \times E_{ff}$ as coming from the combination of temperature-dependent $E_{\rm g}$ and thermal spectral broadening. The relatively small negative thermal quenching of Yb³+:CsPbCl₃ and nearby compositions with when $E_{\rm g} > 2 \times E_{ff}$ may reflect thermal acceleration of energy transfer from the intermediate defect state as identified previously.²5

Yb³⁺ Sensitization below the Quantum-Cutting Energy Threshold. The sensitization mechanism operative in Yb³⁺:CsPbBr₃ deserves special mention because in this case E_g is well below $2 \times E_{f:f}$ so only a single-ion sensitization mechanism may be feasible. The energy mismatch between donor (E_g) and acceptor (single $|^2F_{5/2}\rangle \rightarrow |^2F_{7/2}\rangle$) transitions in this case is very large (\sim 10000 cm⁻¹), however, and for energy conservation must be compensated, e.g., by non-radiative multiphonon emission or Auger-type carrier excitation.

Figure 5a compares the 5 K steady-state NIR PL spectra of 0.2% Yb³⁺:CsPbCl₃ and 7.8% Yb³⁺:CsPbBr₃ NCs. The complex Yb³⁺:CsPbCl₃ spectrum has been discussed previously in terms of a combination of crystal-field and vibronic contributions.²⁵ The Yb³⁺:CsPbBr₃ spectrum has not been

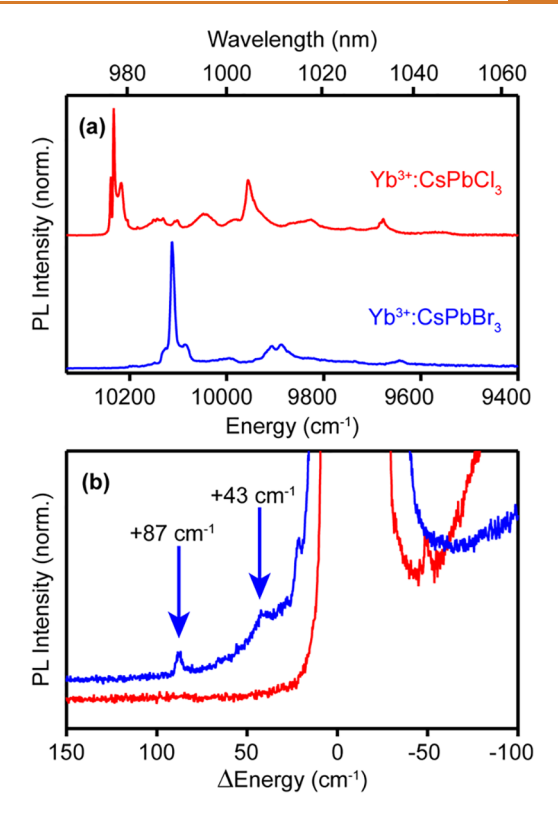


Figure 5. (a) 5 K PL spectra of 0.2% Yb³⁺:CsPbCl₃ (red) and 7.8% Yb³⁺:CsPbBr₃ (blue) NCs. (b) PL spectra in panel (a), magnified and replotted on an energy axis relative to the first electronic origins. The spectra in (b) are both normalized at peak maxima of 10233 and 10113 cm⁻¹ for Yb³⁺:CsPbCl₃ and Yb³⁺:CsPbBr₃, respectively. The arrows mark hot bands at $\Delta E = 43$ and 87 cm⁻¹ in the Yb³⁺:CsPbBr₃ spectrum. $\lambda_{\rm ex} = 375$ nm (26700 cm⁻¹) for both samples.

reported previously. This spectrum shows a narrow peak at 10113 cm⁻¹, interpreted as the $\Gamma_8 \rightarrow \Gamma_6$ electronic origin (zero-phonon line, compared with the similar peak at 10233 cm⁻¹ in Yb³⁺:CsPbCl₃). The energy difference between these Cl and Br peaks is similar to that observed between Yb³⁺doped Cs₂NaHoCl₆ (10248 cm⁻¹) and Cs₂NaHoBr₆ (10144 cm⁻¹).³⁹ Yb³⁺:CsPbCl₃ shows a low-symmetry splitting of the emissive $\Gamma_8(^2F_{5/2})$ level into 0' and 1' crystal-field components. Similarly, we tentatively assign the Yb3+:CsPbBr3 peaks at 9907 and 9886 cm-1 to the split $\Gamma_8(^2F_{7/2})$ level. This splitting (21 cm⁻¹) is comparable to those in other bromide lattices (e.g., 26 cm⁻¹ in Cs₃Yb₂Br₉³⁵ and 52 cm⁻¹ in CsCdBr₃).⁴⁰ The peak at 9645 cm⁻¹ is tentatively assigned to the $0' \rightarrow 3$ transition, which is again similar to those in related lattices (9678 and 9658 cm⁻¹ in $Cs_3Yb_2Br_9^{35}$ and CsCdBr₃, ⁴⁰ respectively). The Yb³⁺ crystal-field splittings in CsPbBr₃ are thus similar to those in Cs₂NaHoBr₆, 99 Cs₃Yb₂Br₉, 35 and CsCdBr₃, 40 indicating a similar [YbBr₆]^{3–} structure.

Figure 5b plots the same two spectra on expanded energy and intensity scales, where the energy axis is now referenced to the first electronic origin in each spectrum. The Yb³⁺:CsPbBr₃ NC spectrum shows two weak features at $\Delta E = +43$ and +87 cm⁻¹ that have no analogue in the Yb³⁺:CsPbCl₃ spectrum. These features both increase in intensity with increasing temperature relative to the first electronic origin (see Figure S17) and are thus assigned as "hot" sidebands.

Figure 6 shows gated PL spectra of the Yb³⁺:CsPbBr₃ NCs measured at 5 K and collected in 500 ns integration windows

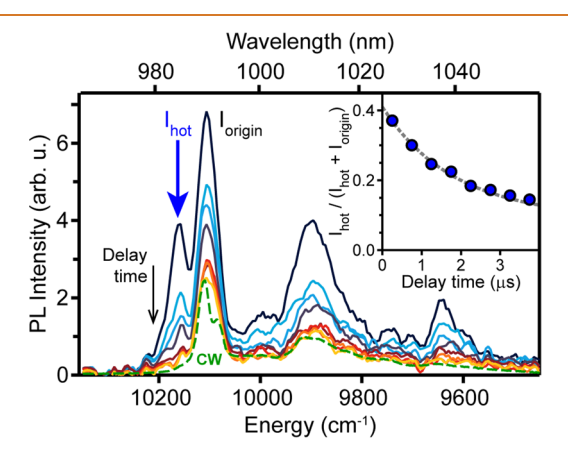


Figure 6. PL spectrum of the Yb³+:CsPbBr₃ NCs from Figure 5a measured at 5 K using CW excitation (green dashed), compared to gated PL spectra collected under the same conditions over the first 4 μ s of decay following a 40 ps laser pulse (solid, $\lambda_{\rm ex}$ = 355 nm (28200 cm⁻¹)). Each gated spectrum was integrated over a 500 ns interval. Inset: The ratio of integrated hot-band (10156 cm⁻¹) to first-electronic-origin (10113 cm⁻¹) PL intensities from the gated PL spectra, plotted as a function of delay time after the photoexcitation pulse. The data points mark the centers of the 500 ns integration periods for each delay time. The gray dashed trace shows an exponential fit of the ratio. The spectral bandwidth is \sim 11 cm⁻¹.

at different delay times over the first 4 μ s following 40 ps of excitation of the perovskite (Figure S18). Because of the slow emission by Yb3+, these gated spectra could not be collected with the same spectral resolution as the CW PL spectra in Figure 5. Nonetheless, the spectrum collected in the first 500 ns window following excitation shows a dramatic increase in the relative intensity of a feature on the high-energy side of the first electronic origin ($\Delta E \approx +50 \text{ cm}^{-1}$), attributed to the same hot bands as seen in Figure 5b. Note that this hot-band intensity is independent of excitation power under these conditions (Figure S20), showing that it is intrinsic to the excitation process. With increasing delay time, the intensity of this peak decreases, and its maximum red-shifts slightly to align with the ~43 cm⁻¹ feature seen in the CW spectrum of Figure 5b. The peak is almost no longer discernible in the spectrum integrated from 3.5 to 4.0 μ s. By that time, the spectrum resembles the CW PL spectrum of these Yb³⁺:CsPbBr₃ NCs (Figure 5). The inset of Figure 6 plots the ratio of I_{hot} to (I_{origin} + $I_{\rm hot}$) as a function of the delay time after excitation. $I_{\rm hot}/$ $(I_{\text{origin}} + I_{\text{hot}})$ decreases exponentially, approaching the 5 K steady-state value obtained with low-power CW photoexcitation at long times (Figure S19). Similar hot bands can be seen for other features throughout the spectrum, but with poorer clarity due to overlapping peaks. These observations suggest extensive local heating of the emissive Yb3+, followed by internal cooling with a time constant of $\sim 2 \mu s$. To estimate the Yb3+ internal temperature, the data in Figure 6 are compared with CW VTPL spectra of the same NCs (Figure S17b). In the VTPL data, the hot band intensities are reliably quantifiable only up to ~70 K, where the thermal contribution to $I_{\rm hot}/(I_{\rm origin}+I_{\rm hot})$ is ${\sim}0.20$ (using $I_{\rm hot}=I_{+43}+I_{+87}$). The value of $I_{\rm hot}/(I_{\rm origin}+I_{\rm hot})\sim 0.40$ at t=0 in Figure 6 thus indicates an initial Yb³⁺ internal temperature well over 100 K,

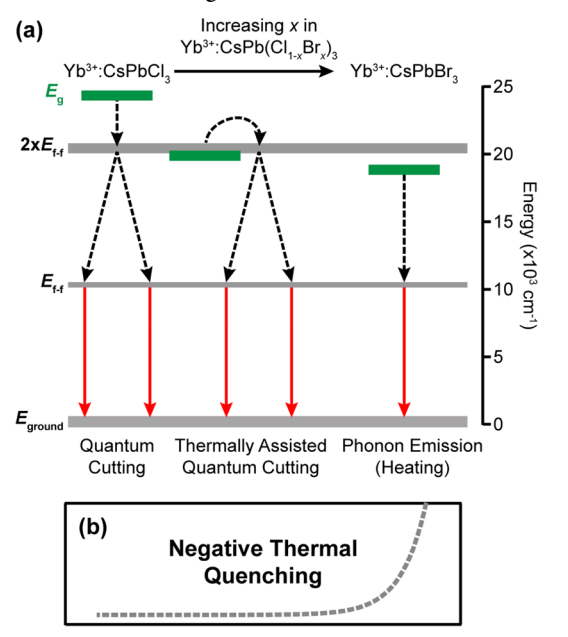
and likely several hundred degrees Kelvin. A more precise determination of the internal temperature at short times is unreliable, because of the high internal temperatures involved.

These results highlight that at 5 K, Yb³⁺ sensitization in Yb³⁺:CsPbBr₃ is dominated by direct perovskite-to-Yb³⁺ energy transfer (not quantum cutting), accompanied by nonradiative multiphonon emission of the excess ~10000 cm⁻¹ per energy-transfer event, which leads to massive Yb³⁺ local heating. No similar local heating is observed in Yb³⁺:CsPbCl₃ (Figures 5b and S21), reflecting the change in sensitization mechanism above the quantum-cutting energy threshold and emphasizing the much greater *energy* efficiency of the quantum-cutting mechanism.

As described above, the integrated Yb3+ PL increases by ~135 times with increasing temperature, attributable to the onset of small but nonzero spectral overlap for resonant concerted quantum cutting. This interpretation is supported by the Yb3+ PL decay traces measured for these Yb3+:CsPbBr3 NCs. Unlike in Yb3+:CsPbCl3 NCs,25 the Yb3+ PL of Yb3+:CsPbBr3 NCs does not show any discernible Yb3+ PL rise time at 5 K but instead primarily decays with a fast time constant (~10s of ns, Figure S18), tentatively attributed to the effects of local heating. With increasing temperature, the decay curves grow increasingly similar to those of Yb³⁺:CsPbCl₃ NCs, and by room temperature show slow decay with a rise time of ~10 ns, very similar to Yb³⁺:CsPbCl₃. Critically, although ρ is very small, room-temperature quantum cutting in Yb3+:CsPbBr3 NCs is still >100× more efficient than the phonon-assisted single-Yb3+ sensitization identified at 5 K, highlighting the extreme efficiency of quantum cutting in these materials.

The results presented above provide insights into the unusual photophysics of Yb3+-doped CsPb(Cl_{1-x}Br_x)₃ perovskites by demonstrating a link between the quantum-cutting energy threshold and negative thermal quenching. Scheme 1 summarizes the different mechanistic regimes identified in this study. In regime (i), Yb^{3+} :CsPb($Cl_{1-x}Br_x$)₃ NCs (0.00 $\leq x \leq \sim$ 0.50) have $E_{\rm g} > 2 \times E_{\rm f-f}$ and are capable of quantum cutting at all temperatures with release of excess energy via phonon emission.²⁰ In regime (ii), Yb^{3+} :CsPb($Cl_{1-x}Br_x$)₃ NCs (~0.50 $\leq x \leq \sim 1.00$) have $E_{\rm g} \approx 2 \times E_{\rm f-f}$. At low temperature, these compositions have reduced spectral overlap because their lowest donor transitions occur at energies below the lowest Yb3+-Yb3+ simultaneous-pair absorption transitions and therefore cannot contribute. Compositions in this regime show improved quantum cutting at elevated temperatures with the assistance of thermal band-gap widening and line broadening, manifested as strong negative thermal quenching of Yb³⁺ PL. In regime (iii), Yb^{3+} :CsPb(Cl_{1-x}Br_x)₃ NCs (~0.80 $\leq x \leq$ ~ 1.00) at low temperature have effectively no donor/acceptor spectral overlap and thus show no quantum cutting. In this regime, energy transfer from the perovskite to Yb³⁺ involves an inefficient nonresonant single-Yb3+ process that requires massive phonon emission to dissipate ~10000 cm⁻¹ per energy-transfer event. This excess energy heats the sample, with internal temperatures of Yb3+ likely reaching hundreds of degrees Kelvin when measured at a cryostat temperature of 5 K. For compositions in regimes (ii) and (iii), elevated temperatures broaden the donor and acceptor spectra and blue-shift the excitonic PL energy, rapidly increasing the spectral overlap required for resonant quantum cutting and causing strong negative thermal quenching of Yb³⁺ PL.

Scheme 1. (a) Quantum-Cutting Energy Transfer in Yb^{3+} :CsPb(Cl_{1-x}Br_x)₃ NCs for Three Distinct Scenarios of E_g Relative to $2 \times E_{ff}$ with Increasing x in Yb^{3+} :CsPb(Cl_{1-x}Br_x)₃ NCs, and (b) Summary of the Experimental Trend in Negative Thermal Quenching of Yb^{3+} PL with Increasing x



CONCLUSION

In summary, we report the observation of strong negative thermal quenching in Yb³⁺:CsPb(Cl_{1-x}Br_x)₃ NCs (0.00 $\leq x \leq$ 1.00). Data analysis and modeling conclusively show that this phenomenon stems from the temperature dependence of quantum cutting. The probability of quantum cutting is modeled in terms of the spectral overlap between donor (perovskite) PL and acceptor (Yb3+-Yb3+) simultaneous pair absorption, which becomes strongly temperature dependent for compositions approaching CsPbBr3. In the limit of Yb3+:CsPbBr3, the dominant energy-transfer mechanism itself changes between 5 K (nonresonant single-ion excitation compensated by multiphonon emission) and room temperature (quantum cutting), resulting in the most dramatic negative thermal quenching of Yb^{3+} PL, with intensities increasing by $>10^2$ over this temperature range. These results advance our fundamental understanding of the photophysical properties of Yb³⁺:CsPb(Cl_{1-x}Br_x)₃ quantum cutters and provide a more detailed quantitative assessment of the quantum-cutting mechanism than reported previously, aiding and informing further development of these materials for future solar and photonic applications.

METHODS

Materials. Oleic acid (OA, 90%, Sigma-Aldrich), 1-octadecene (ODE, 90%, Sigma-Aldrich), oleylamine (OAm, 70%, Sigma-Aldrich), lead acetate trihydrate (Pb(OAc)₂·3H₂O, 99.999%, Sigma-Aldrich), cesium acetate (CsOAc, 99.9%, Sigma-Aldrich), anhydrous ethanol (EtOH, 200 proof, Decon Laboratories, Inc.), trimethylsilyl chloride (TMS-Cl, 99%, Sigma-Aldrich), trimethylsilyl bromide (TMS-Br, 97%, Sigma-Aldrich), *n*-hexane (99%, Sigma-Aldrich), and ethyl acetate (EtOAc, 99%, Sigma-Aldrich) were used as received unless otherwise noted. As-received ytterbium acetate hydrate (Yb(OAc)₃· xH₂O, 99.9%, Alfa Aesar) was refluxed in glacial acetic acid for 1 h and stored in a desiccator prior to use.

Nanocrystal Synthesis. Doped $CsPbX_3$ (X = Cl, Br) NCs were synthesized as detailed previously. 13 In a typical synthesis, Yb(OAc)3 (1–12 mg), Pb(OAc)₂·3H₂O (76 mg), ODE (5.0 mL), OA (1.0 mL), OAm (0.25 mL), and 1 M CsOAc in EtOH (0.28 mL) were combined in an oven-dried round-bottomed flask and degassed on a Schlenk line for 1 h at 110 °C. The vessel was then flushed with N₂ and heated to 240 °C, whereupon a room-temperature TMS-X solution prepared in a nitrogen-filled glovebox (0.2 mL of TMS-X and 0.5 mL of anhydrous ODE) was injected. Following the injection, the reaction vessel was immediately cooled using a room-temperature water bath. The reaction vessel with the resulting NC solution was transferred to a nitrogen-filled glovebox, where the solution was centrifuged at 6000 rpm for 10 min. The supernatant was discarded, leaving a white Yb3+-doped CsPbCl3 or a yellow Yb3+-doped CsPbBr3 NC pellet. The NC pellet was resuspended in n-hexane and flocculated out of the solution with EtOAc. The suspension then was centrifuged again for 10 min, and the supernatant was discarded. The resulting pellet was resuspended in *n*-hexane and centrifuged for another 15 min. The supernatant, this time, containing NCs was stored in anhydrous hexane in a nitrogen glovebox.

Nanocrystal Pellet Preparation. Multiple batches of Yb³+-doped CsPbCl₃ NCs in hexane were flocculated out of the solution with EtOAc and centrifuged for 20 min, and the supernatant was discarded. The resulting pellet was dried under nitrogen air and broken into powder in mortal and pestle. The resulting powder (~0.2 g) was loaded onto a pellet die and pressed at 8 tons for about 2 min under vacuum.

Anion Exchange. Doped $CsPb(Cl_{1-x}Br_x)_3$ NCs were prepared by anion exchange using Yb^{3+} : $CsPbCl_3$ NCs according to protocols as detailed previously. 20,29,30 In short, the NC solution stored in a nitrogen glovebox was titrated with 1 M TMS-Br until the desired band gap was achieved, as determined by PL spectroscopy at room temperature. The residual TMS-Br and solvent were removed by vacuum evaporation, and the resulting NCs were then resuspended in anhydrous hexane and stored in a nitrogen glovebox. $\sim 30\%$ of the Yb^{3+} : $CsPbCl_3$ NC pellet was anion exchanged to achieve the desired bandgap $(Yb^{3+}:CsPb(Cl_{0.25}Br_{0.75})_3)$ via gas-phase anion exchange using neat TMS-Br in a nitrogen-filled glovebox. The anion-exchanged NC powder was loaded onto a pellet die and pressed at 8 tons under vacuum.

Physical Characterization. TEM images were obtained using an FEI TECNAI F20 microscope operating at 200 kV. TEM samples were prepared by drop-casting NCs onto ultrathin carbon-coated copper grids from TED Pella, Inc. Elemental composition of the NC samples was determined using inductively coupled plasma-atomic emission spectroscopy (ICP-AES, PerkinElmer 8300). NC samples were prepared by digesting NC powders in concentrated nitric acid overnight with ultrasonication. Then, the nitric acid mixture was diluted in ultrapure H_2O . All dopant concentrations in perovskites were determined as the B-site cation mole fraction (in %). pXRD data were collected using a Bruker D8 Discover diffractometer with a high-efficiency $I\mu$ S microfocus X-ray source for Cu K α radiation (50 kV, 1 mA). Samples for XRD measurements were prepared by dropcasting NCs onto a silicon substrate.

Spectroscopic Measurements. Samples for variable-temperature NIR absorption measurements were cooled to 5 K in a helium flow cryostat. All absorption spectra were collected using an Agilent Cary 5000 spectrometer operation in transmission mode. Samples for PL and gated PL measurements were prepared by drop-casting NCs onto quartz disks that were cooled to 4.5 K in a closed-cycle helium cryostat (Janis, SHI-4H-5). PL spectra were measured at each temperature using a 375 nm light-emitting diode (LED) for excitation, operating at ~0.6 mW/cm². PL data were measured using a LN₂-cooled silicon charge-coupled device (CCD) camera mounted on a monochromator with a spectral bandwidth of about 0.38 nm (~3.87 cm⁻¹) and 0.03 nm (~0.31 cm⁻¹) for variable-temperature and high-resolution PL data, respectively. All luminescence spectra are displayed as photon counts versus energy (cm⁻¹) following appropriate conversion.

For time-resolved PL measurements, photoexcitation was provided by an Ekspla Nd:yttrium aluminum garnet laser (355 nm) firing at a repetition rate of 50 Hz with a 40 ps pulse width. The excitation energy was held at $\sim\!\!35~\mu\mathrm{J/cm^2}$ per pulse. The NIR PL signals were focused into a monochromator, detected by a Hamamatsu InGaAs/InP NIR photomultiplier tube, and recorded by using either a multichannel scalar (Stanford Research Systems SR430) or a gated photon counter (Stanford Research Systems, SR400). A spectral bandwidth of 1.10 nm ($\sim\!\!11~\mathrm{cm^{-1}})$ was used for all time-resolved PL measurements.

Photoluminescence excitation (PLE) spectra were measured at room temperature by using an Edinburgh FLS 1000 photoluminescence spectrometer equipped with a 450 W xenon lamp as an excitation source, detected by a Hamamatsu InGaAs/InP NIR photomultiplier with a spectral bandwidth of 1 nm (~10 cm⁻¹).

ASSOCIATED CONTENT

5 Supporting Information

The Supporting Information is available free of charge at https://pubs.acs.org/doi/10.1021/acsnano.3c05053.

Additional TEM images, XRD data, VT-absorption, VTPL, time-resolved PL, gated PL spectra, and scatter plots (PDF)

AUTHOR INFORMATION

Corresponding Author

Daniel R. Gamelin — Department of Chemistry, University of Washington, Seattle, Washington 98195, United States; orcid.org/0000-0003-2888-9916; Email: gamelin@uw.edu

Authors

Joo Yeon D. Roh — Department of Chemistry, University of Washington, Seattle, Washington 98195, United States; orcid.org/0000-0001-9801-3069

Tyler J. Milstein – Department of Chemistry, University of Washington, Seattle, Washington 98195, United States; orcid.org/0000-0002-1517-2222

Complete contact information is available at: https://pubs.acs.org/10.1021/acsnano.3c05053

Notes

The authors declare no competing financial interest.

ACKNOWLEDGMENTS

This work was primarily supported by the U.S. National Science Foundation through the University of Washington Molecular Engineering Materials Center, a Materials Research Science and Engineering Center (DMR-1719797). Early stages of this work were performed with the support of NSF DMR-1807394. Part of this work was conducted at the University of Washington Molecular Analysis Facility, a National Nanotechnology Coordinated Infrastructure site supported in part by funds from the National Science Foundation (awards NNCI-2025489 and NNCI-1542101), the Molecular Engineering & Sciences Institute, and the Clean Energy Institute. The authors thank J. J. Araujo for acquiring XRD data and K. T. Kluherz for acquiring TEM images.

REFERENCES

(1) Wegh, R. T.; Donker, H.; Oskam, K. D.; Meijerink, A. Visible Quantum Cutting in LiGdF₄:Eu³⁺ Through Downconversion. *Science* **1999**, 283, 663–666.

- (2) Vergeer, P.; Vlugt, T. J. H.; Kox, M. H. F.; den Hertog, M. I.; van der Eerden, J. P. J. M.; Meijerink, A. Quantum Cutting by Cooperative Energy Transfer in Yb_xY_{1-x}PO₄:Tb³⁺. *Phys. Rev. B* **2005**, *71*, 014119.
- (3) Chen, D.; Wang, Y.; Yu, Y.; Huang, P.; Weng, F. Near-Infrared Quantum Cutting in Transparent Nanostructured Glass Ceramics. *Opt. Lett.* **2008**, 33, 1884–1886.
- (4) Van der Ende, B. M.; Aarts, L.; Meijerink, A. Near-Infrared Quantum Cutting for Photovoltaics. *Adv. Mater.* **2009**, *21*, 3073–3077.
- (5) Eilers, J. J.; Biner, D.; van Wijngaarden, J. T.; Krämer, K.; Güdel, H.-U.; Meijerink, A. Efficient Visible to Infrared Quantum Cutting Through Downconversion with the Er³⁺–Yb³⁺ Couple in Cs₃Y₂Br₉. *Appl. Phys. Lett.* **2010**, *96*, 151106.
- (6) Shockley, W.; Queisser, H. J. Detailed Balance Limit of Efficiency of *p-n* Junction Solar Cells. *J. Appl. Phys.* **1961**, 32, 510–519.
- (7) Dexter, D. L. Two Ideas on Energy Transfer Phenomena: Ion-Pair Effects Involving the OH Stretching Mode, and Sensitization of Photovoltaic Cells. *J. Lumin.* **1979**, *18*–*19*, 779–784.
- (8) Trupke, T.; Green, M. A.; Würfel, P. Improving Solar Cell Efficiencies by Down-Conversion of High-Energy Photons. *J. Appl. Phys.* **2002**, 92, 1668–1674.
- (9) Hanna, M. C.; Nozik, A. J. Solar Conversion Efficiency of Photovoltaic and Photoelectrolysis Cells with Carrier Multiplication Absorbers. *J. Appl. Phys.* **2006**, *100*, 074510.
- (10) Nozik, A. J.; Beard, M. C.; Luther, J. M.; Law, M.; Ellingson, R. J.; Johnson, J. C. Semiconductor Quantum Dots and Quantum Dot Arrays and Applications of Multiple Exciton Generation to Third-Generation Photovoltaic Solar Cells. *Chem. Rev.* **2010**, *110*, 6873–6890.
- (11) Pan, G.; Bai, X.; Yang, D.; Chen, X.; Jing, P.; Qu, S.; Zhang, L.; Zhou, D.; Zhu, J.; Xu, W.; et al. Doping Lanthanide into Perovskite Nanocrystals: Highly Improved and Expanded Optical Properties. *Nano Lett.* **2017**, *17*, 8005–8011.
- (12) Kroupa, D. M.; Roh, J. Y.; Milstein, T. J.; Creutz, S. E.; Gamelin, D. R. Quantum-Cutting Ytterbium-Doped $CsPb(Cl_{1-x}Br_x)_3$ Perovskite Thin Films with Photoluminescence Quantum Yields over 190. ACS Energy Lett. **2018**, 3, 2390–2395.
- (13) Milstein, T. J.; Kroupa, D. M.; Gamelin, D. R. Picosecond Quantum Cutting Generates Photoluminescence Quantum Yields Over 100% in Ytterbium-Doped CsPbCl₃ Nanocrystals. *Nano Lett.* **2018**, *18*, 3792–3799.
- (14) Mir, W. J.; Mahor, Y.; Lohar, A.; Jagadeeswararao, M.; Das, S.; Mahamuni, S.; Nag, A. Postsynthesis Doping of Mn and Yb into CsPbX₃ (X = Cl, Br, or I) Perovskite Nanocrystals for Downconversion Emission. *Chem. Mater.* **2018**, *30*, 8170–8178.
- (15) Zhang, X.; Zhang, Y.; Zhang, X.; Yin, W.; Wang, Y.; Wang, H.; Lu, M.; Li, Z.; Gu, Z.; Yu, W. W. Yb³⁺ and Yb³⁺/Er³⁺ Doping for Near-Infrared Emission and Improved Stability of CsPbCl₃ Nanocrystals. *J. Mater. Chem. C* **2018**, *6*, 10101–10105.
- (16) Cohen, T. A.; Milstein, T. J.; Kroupa, D. M.; MacKenzie, J. D.; Luscombe, C. K.; Gamelin, D. R. Quantum-Cutting Yb³⁺-Doped Perovskite Nanocrystals for Monolithic Bilayer Luminescent Solar Concentrators. *J. Mater. Chem. A* **2019**, *7*, 9279–9288.
- (17) Crane, M. J.; Kroupa, D. M.; Roh, J. Y.; Anderson, R. T.; Smith, M. D.; Gamelin, D. R. Single-Source Vapor Deposition of Quantum-Cutting Yb³⁺:CsPb(Cl_{1-x}Br_x)₃ and Other Complex Metal-Halide Perovskites. ACS Appl. Energy Mater. 2019, 2, 4560–4565.
- (18) Erickson, C. S.; Crane, M. J.; Milstein, T. J.; Gamelin, D. R. Photoluminescence Saturation in Quantum-Cutting Yb³⁺-Doped CsPb($\text{Cl}_{1-x}\text{Br}_x$)₃ Perovskite Nanocrystals: Implications for Solar Downconversion. *J. Phys. Chem. C* **2019**, *123*, 12474–12484.
- (19) Luo, X.; Ding, T.; Liu, X.; Liu, Y.; Wu, K. Quantum-Cutting Luminescent Solar Concentrators Using Ytterbium-Doped Perovskite Nanocrystals. *Nano Lett.* **2019**, *19*, 338–341.
- (20) Milstein, T. J.; Kluherz, K. T.; Kroupa, D. M.; Erickson, C. S.; De Yoreo, J. J.; Gamelin, D. R. Anion Exchange and the Quantum-

- Cutting Energy Threshold in Ytterbium-Doped CsPb(Cl_{1-x}Br_x)₃ Perovskite Nanocrystals. Nano Lett. 2019, 19, 1931-1937.
- (21) Zhou, D.; Sun, R.; Xu, W.; Ding, N.; Li, D.; Chen, X.; Pan, G.; Bai, X.; Song, H. Impact of Host Composition, Codoping, or Tridoping on Quantum-Cutting Emission of Ytterbium in Halide Perovskite Quantum Dots and Solar Cell Applications. Nano Lett. 2019, 19, 6904-6913.
- (22) Cai, T.; Wang, J.; Li, W.; Hills-Kimball, K.; Yang, H.; Nagaoka, Y.; Yuan, Y.; Zia, R.; Chen, O. Mn²⁺/Yb³⁺ Codoped CsPbCl₃ Perovskite Nanocrystals with Triple-Wavelength Emission for Luminescent Solar Concentrators. Adv. Sci. 2020, 7, 2001317.
- (23) Ding, N.; Xu, W.; Zhou, D.; Ji, Y.; Wang, Y.; Sun, R.; Bai, X.; Zhou, J.; Song, H. Extremely Efficient Quantum-Cutting Cr³⁺, Ce³⁺ Yb3+ Tridoped Perovskite Quantum Dots for Highly Enhancing the Ultraviolet Response of Silicon Photodetectors with External Quantum Efficiency Exceeding 70. Nano Energy 2020, 78, 105278.
- (24) Ishii, A.; Miyasaka, T. Sensitized Yb3+ Luminescence in CsPbCl₃ Film for Highly Efficient Near-Infrared Light-Emitting Diodes. Adv. Sci. 2020, 7, 1903142.
- (25) Roh, J. Y. D.; Smith, M. D.; Crane, M. J.; Biner, D.; Milstein, T. J.; Krämer, K. W.; Gamelin, D. R. Yb3+ Speciation and Energy-Transfer Dynamics in Quantum-Cutting Yb3+-Doped CsPbCl3 Perovskite Nanocrystals and Single Crystals. Phys. Rev. Mater. 2020, 4, 105405.
- (26) Zeng, M.; Artizzu, F.; Liu, J.; Singh, S.; Locardi, F.; Mara, D.; Hens, Z.; Van Deun, R. Boosting the Er³⁺ 1.5 μ m Luminescence in CsPbCl₃ Perovskite Nanocrystals for Photonic Devices Operating at Telecommunication Wavelengths. ACS Appl. Nano Mater. 2020, 3, 4699-4707.
- (27) Li, D.; Chen, G. Near-Infrared Photoluminescence from Ytterbium- and Erbium-Codoped CsPbCl₃ Perovskite Quantum Dots with Negative Thermal Quenching. J. Phys. Chem. Lett. 2023, 14, 2837-2844.
- (28) Li, H.; Liu, X.; Zhou, D.; Dong, B.; Xu, L.; Bai, X.; Song, H. Realization of 1.54-μm Light-Emitting Diodes Based on Er³⁺/Yb³⁺Co-Doped CsPbCl₃ Films. Adv. Mater. 202335, 2300118.
- (29) Creutz, S. E.; Crites, E. N.; De Siena, M. C.; Gamelin, D. R. Anion Exchange in Cesium Lead Halide Perovskite Nanocrystals and Thin Films Using Trimethylsilyl Halide Reagents. Chem. Mater. 2018, 30, 4887-4891.
- (30) Creutz, S. E.; Crites, E. N.; De Siena, M. C.; Gamelin, D. R. Colloidal Nanocrystals of Lead-Free Double-Perovskite (Elpasolite) Semiconductors: Synthesis and Anion Exchange To Access New Materials. Nano Lett. 2018, 18, 1118-1123.
- (31) De Siena, M. C.; Sommer, D. E.; Creutz, S. E.; Dunham, S. T.; Gamelin, D. R. Spinodal Decomposition During Anion Exchange in Colloidal Mn^{2+} -Doped CsPbX₃ (X = Cl, Br) Perovskite Nanocrystals. Chem. Mater. 2019, 31, 7711-7722.
- (32) Han, Q.; Wu, W.; Liu, W.; Yang, Q.; Yang, Y. Temperature-Dependent Photoluminescence of CsPbX₃ Nanocrystal Films. J. Lumin. 2018, 198, 350-356.
- (33) Milstein, T. J.; Roh, J. Y. D.; Jacoby, L. M.; Crane, M. J.; Sommer, D. E.; Dunham, S. T.; Gamelin, D. R. Ubiquitous Near-Band-Edge Defect State in Rare-Earth-Doped Lead-Halide Perovskites. Chem. Mater. 2022, 34, 3759-3769.
- (34) Ovsyankin, V. V., CHAPTER 7 Spectroscopy of Collective States and Cooperative Transitions in Disordered Rare-Earth Activated Solids. In Modern Problems in Condensed Matter Sciences, Kaplyanskii, A. A.; Macfarlane, R. M., Eds. Elsevier: 1987; Vol. 21, pp 343-480.
- (35) Hehlen, M. P.; Güdel, H. U. Optical Spectroscopy of the Dimer System Cs₃Yb₂Br₉. J. Chem. Phys. **1993**, 98, 1768–1775.
- (36) Miyakawa, T.; Dexter, D. L. Cooperative and Stepwise Excitation of Luminescence: Trivalent Rare-Earth Ions in Yb3+-Sensitized Crystals. Phys. Rev. B 1970, 1, 70-80.
- (37) Kushida, T. Energy Transfer and Cooperative Optical Transitions in Rare-Earth Doped Inorganic Materials. I. Transition Probability Calculation. J. Phys. Soc. Jpn. 1973, 34, 1318-1326.

- (38) Sommer, D. E.; Gamelin, D. R.; Dunham, S. T. Defect Formation in Yb-Doped CsPbCl₃ from First Principles with Implications for Quantum Cutting. Phys. Rev. Mater. 2022, 6, 025404.
- (39) Tanner, P. A. Electronic Spectra of Yb³⁺ in Elpasolite Lattices. Mol. Phys. 1986, 58, 317-328.
- (40) Hehlen, M. P.; Kuditcher, A.; Rand, S. C.; Tischler, M. A. Electron-Phonon Interactions in CsCdBr₃:Yb³⁺. J. Chem. Phys. 1997, 107, 4886-4892.
- (41) Ejder, E. Methods of Representing Emission, Excitation, and Photoconductivity Spectra. J. Opt. Soc. Am. 1969, 59, 223 1-224.
- (42) Mooney, J.; Kambhampati, P. Get the Basics Right: Jacobian Conversion of Wavelength and Energy Scales for Quantitative Analysis of Emission Spectra. J. Phys. Chem. Lett. 2013, 4, 3316–3318.